NEUROSCIENCE

A bioresorbable peripheral nerve stimulator for electronic pain block

Geumbee Lee[1,2]†, Emily Ray[3,4]†, Hong-Joon Yoon[1]†, Sabrina Genovese[4], Yeon Sik Choi[1], Min-Kyu Lee[1], Samet Şahin[1,5], Ying Yan[4], Hak-Young Ahn[1], Amay J. Bandodkar[6,7], Joohee Kim[1], Minsu Park[1], Hanjun Ryu[8], Sung Soo Kwak[9], Yei Hwan Jung[10], Arman Odabas[4,11], Umang Khandpur[4], Wilson Z. Ray[3,4], Matthew R. MacEwan[3,4]*, John A. Rogers[1,12,13,14,15]*

Local electrical stimulation of peripheral nerves can block the propagation of action potentials, as an attractive alternative to pharmacological agents for the treatment of acute pain. Traditional hardware for such purposes, however, involves interfaces that can damage nerve tissue and, when used for temporary pain relief, that impose costs and risks due to requirements for surgical extraction after a period of need. Here, we introduce a bioresorbable nerve stimulator that enables electrical nerve block and associated pain mitigation without these drawbacks. This platform combines a collection of bioresorbable materials in architectures that support stable blocking with minimal adverse mechanical, electrical, or biochemical effects. Optimized designs ensure that the device disappears harmlessly in the body after a desired period of use. Studies in live animal models illustrate capabilities for complete nerve block and other key features of the technology. In certain clinically relevant scenarios, such approaches may reduce or eliminate the need for use of highly addictive drugs such as opioids.

INTRODUCTION

Opioids represent one of the most common means to manage acute pain. The misuse and overprescription of these drugs, and specifically severe addictions to them, are the basis of a national crisis that affects public health as well as social and economic welfare (*1*, *2*). In 2019, opioid abuse in the United States led to deaths of 50,000 people and a total economic burden of nearly $100 billion (*3*). These circumstances motivate growing interest in alternative methods for the treatment of pain. Particularly attractive are nonpharmaceutical schemes, such as those that rely on electrical stimulation (*4*–*6*), thermal modulation (*7*, *8*), ultrasound (*9*, *10*), or light (*11*, *12*) exposure to partially or fully block signal propagation along peripheral nerves.

Electrical stimulation represents the most successful of these methods, typically classified into several forms depending on the configuration of the electrodes relative to the targeted nerve. Transcutaneous electrical nerve stimulation (TENS) relies on electric stimuli (i.e., biphasic pulses with amplitudes of 1 to 60 mA, durations of 50 to 200 μs, and frequencies of 1 to 200 Hz) delivered through patch electrodes placed on the skin near the source of pain (*13*, *14*). The resulting electrical paresthesia alleviates pain by distracting the brain from painful stimuli (*15*). Although this form of electrotherapy is noninvasive, the large distances between the electrodes and the targeted nerves limit the efficacy due to the insulating effects of the skin and muscle/fat interlayers. Percutaneous electrical nerve stimulation (PENS) overcomes this disadvantage through the use of electrodes that penetrate the skin to deliver electrical stimuli (i.e., biphasic pulses with amplitudes of 0.2 to 20 mA, durations of 15 to 200 μs, and frequencies of 2 to 100 Hz) in proximity to the nerves (*16*, *17*). This method can effectively block nerve conduction, but temporary pain and tissue disruption can occur during and after electrode insertion. In addition, inaccurate positioning can lead to damage to the nerve itself. The most effective approach uses electrodes in cylindrical cuff geometries to deliver kilohertz-frequency alternating current (KHFAC) (i.e., sinusoidal waveforms with an amplitude of 10 V_{pp} and frequencies of 25 to 35 kHz as the optimal condition) directly to the peripheral nerves. The KHFAC stimulation maintains dynamic steady-state depolarization, thereby arresting action potentials in the axons that carry pain signals when they reach the depolarizing charge field (*18*, *19*). This scheme is attractive relative to TENS or PENS because it can reliably and completely block nerve conduction with response times less than 10 ms (*19*, *20*) that are much faster than these alternatives (seconds) (*19*, *21*). A major disadvantage of conventional cuff electrodes for KHFAC stimulation, however, is in complex surgical procedures necessary for implantation and, if necessary, for subsequent removal, with associated risks for additional pain and discomfort, and possible permanent damage to the nerve. In addition, implantation of nonbioresorbable, stiff nerve cuffs can lead to inflammatory cell infiltration and morphological changes (e.g., fibrous capsule) to the nerve as part of the mechanisms that protect nerve functionality from foreign body reactions. These processes result in difficulties in safe removal of a cuff electrode from the nerve (*22*, *23*).

Here, we introduce a thin, flexible bioresorbable cuff technology for KHFAC nerve block, where direct electrode-nerve contact enables

[1]Querrey Simpson Institute for Bioelectronics, Northwestern University, Evanston, IL 60208, USA. [2]Precision Biology Research Center, Sungkyunkwan University, Suwon 16419, Republic of Korea. [3]Department of Biomedical Engineering, Washington University in St. Louis, St. Louis, MO 63130, USA. [4]Department of Neurological Surgery, Washington University School of Medicine in St. Louis, St. Louis, MO 63110, USA. [5]Department of Bioengineering, Bilecik Şeyh Edebali University, 11230 Bilecik, Merkez/Bilecik, Turkey. [6]Department of Electrical and Computer Engineering, North Carolina State University, Raleigh, NC 27606, USA. [7]Center for Advanced Self-Powered Systems of Integrated Sensors and Technologies (ASSIST), North Carolina State University, Raleigh, NC 27606, USA. [8]Department of Advanced Materials Engineering, Chung-Ang University, Anseong 17546, Republic of Korea. [9]Center for Bionics, Biomedical Research Division, Korea Institute of Science and Technology, Seoul 02792, Republic of Korea. [10]Department of Electronic Engineering, Hanyang University, Seoul 04763, Republic of Korea. [11]Department of Internal Medicine, Stanford University Medical Center, Stanford, CA 94305, USA. [12]Department of Materials Science and Engineering, Northwestern University, Evanston, IL 60208, USA. [13]Department of Mechanical Engineering, Northwestern University, Evanston, IL 60208, USA. [14]Department of Biomedical Engineering, Northwestern University, Evanston, IL 60208, USA. [15]Department of Neurological Surgery, Feinberg School of Medicine, Northwestern University, Chicago, IL 60611, USA.
*Corresponding author. Email: macewanm@wustl.edu (M.R.M.); jrogers@northwestern.edu (J.A.R.)
†These authors contributed equally to this work.

complete, fast operation and natural processes of bioresorption to eliminate the need for surgical removal. Key advances relative to related bioresorbable nerve stimulators for neuroregeneration include (i) multimaterial structures that support high-voltage, high-frequency stimulation over extended time periods, aligned to clinical needs for pain mitigation; (ii) bioresorbable cuffs that exploit woven structure geometries for reliable delivery of KHFAC; (iii) schemes for electrical and mechanical decoupling between the cuff and extension electrodes by selective bioresorption to reduce the potential for damage to the nerve; and (iv) demonstrations of complete, fast, and reversible electronic nerve conduction block in live animal models. These results establish the basis for a temporary, bioelectronic form of medicine for pain management, with potential to replace or complement traditional pharmacological schemes and conventional electrical stimulation approaches.

RESULTS

Overall materials and design strategies

An essential feature of the systems introduced here is that all of the constituent materials are bioresorbable. The electrodes and electrical interconnect traces rely on bioresorbable metals. The encapsulating materials, supporting substrates, and cuff structures exploit bioresorbable polymers. Recent reviews summarize the expanding base of knowledge in these and other classes of physically transient electronic materials (*24*–*26*). A notable challenge in the present context is that the dissolution rates of the stimulation electrodes can be strongly influenced by electrochemical reactions initiated by the application of the electrical bias needed for KHFAC. Previously published simulators for neuroregeneration incorporate bioresorbable electrodes of magnesium (Mg) to support comparatively low-voltage operation (monophasic pulse, 100 to 300 mV) and short periods of use (low–duty cycle operation for hours or days) (*27*, *28*), followed by fast dissolution (decreases in thicknesses of ~4 μm/day) (*29*). Continuous application of electrical biases with waveforms relevant to the application explored here [AC, amplitude: 10 V_{pp}, frequency: 25 kHz; immersion in phosphate-buffered saline (PBS) at 37°C] leads to rapid loss of electrical conductivity of Mg electrodes over time scales that are insufficient to satisfy most clinical requirements in temporary pain mitigation (e.g., stable use for weeks) (fig. S1) (*30*). Molybdenum (Mo), another bioresorbable metal, represents an attractive alternative because of its relatively slow intrinsic rate of dissolution under typical physiological conditions (0.02 μm/day) (*31*).

The designs reported here combine both Mo and Mg in woven structures that exploit the advantages of both. Electrodes of Mo in a cuff structure form a stable interface to the targeted nerve during delivery of blocking stimuli. Extension electrodes of Mg, encapsulated in a bioresorbable polymer that electrically insulates them from surrounding biofluids and reduces their rates of dissolution, serve as connections to an externalized power supply (fig. S2). Optimized choices of materials and geometries cause this part of this system to decouple from the cuff electrode (i.e., Mo) on a time scale comparable to the need for nerve block. This process removes unnecessary mechanical load on the nerve, as the cuff dissolves naturally over a subsequent time period. Thin, flexible, and bioresorbable stimulators block the propagation of pain signals in peripheral nerves.

A woven structure forms a stable interconnection between the Mo and Mg parts of the system. This configuration bypasses mechanically induced failures that often occur with end-to-end connections. An exploded-view illustration in Fig. 1A highlights the layout, in which thin strips of Mo (300 μm wide, 15 μm thick) interleave through three small slits (rectangular layout; 320 μm wide, 20 μm long) in strips of Mg (1 mm wide, 50 μm thick). The bottom right inset shows a side view, and fig. S3 represents the detailed fabrication method. The woven, interleaved region provides not only mechanical strength but also robust electrical contacts, as summarized in quantitative experiments in figs. S3 and S4 (*32*). A coating with conductive wax [C-wax; tungsten (W)/candelilla wax mixture] further fortifies the joint (*33*).

The number, widths, and spacings of the electrodes in the cuff structure influence the effectiveness of the block (*6*). The design reported here uses a tripolar configuration of electrodes of Mo with widths of 300 μm and spacings of 1 mm. According to previous reports on conventional cuff electrodes for KHFAC blocking, bipolar and/or tripolar electrodes can provide an effective block without onset responses (typically in the form of a temporary muscle twitch when KHFAC initiates) (*6*, *34*, *35*). Several previous studies use tripolar nerve cuffs for chronic applications of KHFAC because of their ability to reduce current spreading to neighboring structures during electrical stimulation (*6*, *36*, *37*). For the rat sciatic nerves, the optimal separation between electrodes is in the range of 0.5 to 1 mm (*6*). Successful nerve block can be achieved using electrodes with different widths (i.e., 300, 700, and 1000 μm) (fig. S5).

A ~40-μm-thick layer of poly(lactic-co-glycolic acid) [PLGA; 75:25 (lactide:glycolide)] serves as a support for these electrodes to define the overall cuff geometry. Two layers of polyanhydride (PA; ~200 μm thick) encapsulate the electrodes (*38*), except in those regions that establish the nerve interface. The use of these different polymers offers distinct advantages. The thermoplastic nature of PLGA and its low glass transition temperature (T_g: 40 to 60°C) provide a simple means for thermally joining the overlapping portion in the PLGA support through local heating (~60°C) applied carefully during implantation in a manner that avoids damage to the nerve (fig. S6). In this way, the cuff can be wrapped circumferentially around the nerve to ensure conformal, direct contact. The PA encapsulant serves as a bioresorbable barrier with superior properties compared to those of PLGA to prevent interaction of biofluids with the Mg traces. The complete system (8 mm wide, 400 μm thick) offers thin, flexible mechanical properties that allow the structure to adapt to natural movements after implantation (Fig. 1A, top right inset).

Figure 1B illustrates the use of this bioresorbable nerve cuff structure as a secure electrode-nerve interface. An exposed, ~5-mm length of the Mo electrode serves as a stimulating interface that completely and gently wraps around the nerve to form a cylindrical structure, designed in this case for the sciatic nerve (average diameter of 1.5 mm) of the rat model. The extension electrodes of Mg interface to external equipment that generates electrical waveforms for complete and efficient nerve conduction block.

All constituent materials react via chemical/biochemical processes of hydrolysis and metabolic action, as they resorb into the body (fig. S7) (*32*, *39*, *40*). Figure 1C illustrates the use of the system for pain block and its three constituent parts: (I) extension electrodes (Mg/PA), (II) woven structure (Mo/Mg connection), and (III) nerve cuff (Mo/PLGA). Electrical stimulation waveforms pass from an external generator to the targeted nerve for conduction block and, therefore, pain management. After a period of operation, the interconnects that emerge from the skin can be cut away. Part I dissolves first due to the high rate of bioresorption of Mg that follows from the permeation of water

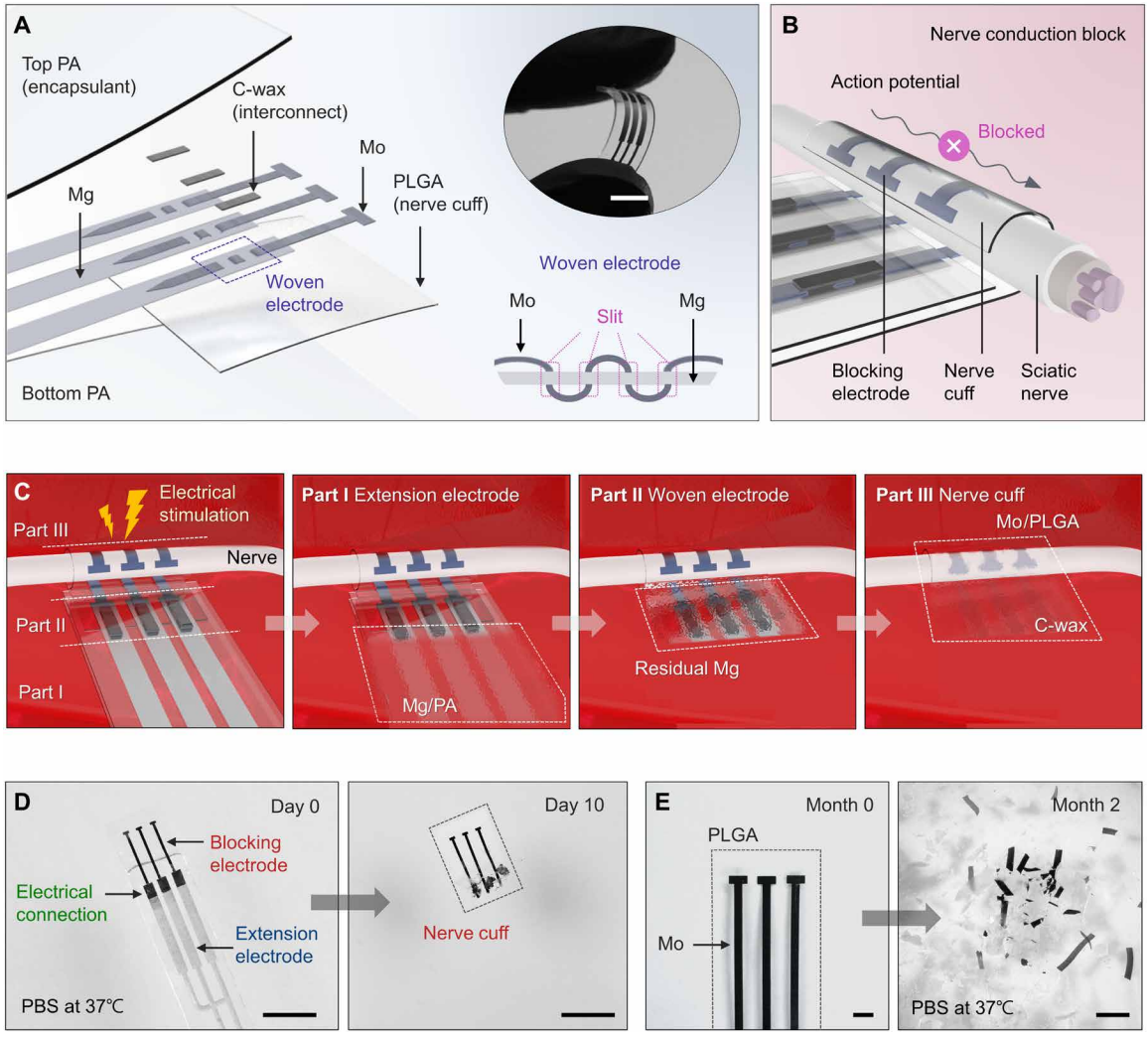

Fig. 1. Materials and designs for a bioresorbable electrical stimulator for nerve conduction block. (**A**) Schematic illustration of a stimulator that consists of mechanically woven interconnects (Mg: 1 mm wide, 50 μm thick; Mo: 300 μm wide, 15 μm thick) to electrodes with a tripolar configuration mounted on a nerve cuff (PLGA, 40 μm thick). All active elements reside between a pair of bioresorbable polymer films (PA, 400 μm thick) except the region of the cuff where exposed electrodes deliver electrical stimulation to the nerve. Top inset: Image of a flexible device bent with the fingertips. Bottom inset: Detailed cross-sectional view of the woven electrode. Scale bar, 10 mm (top inset). (**B**) Schematic illustration of the process of nerve conduction block induced by a bioresorbable electrical stimulator in a cuff geometry. Mo electrodes that wrap around the nerve deliver electrical stimulation to block the conduction of action potential. (**C**) Illustration of the use, release, and bioresorption of the device through various stages of its lifetime. Sequential processes of dissolution engineered by choices in component designs and materials determine the functional and physical lifetimes. A series of images show the process of dissolution of a device during immersion in 1× PBS (pH 7.4) at physiological temperatures (37°C). (**D**) Day 10: Dissolution of the extension electrodes (Mg/PA). Scale bars, 5 mm. (**E**) Month 2: Disintegration and dissolution of the nerve cuff (Mo/PLGA). Scale bars, 1 mm.

through the PA and from direct exposure via dissolution of the PA. This process electrically and mechanically isolates the cuff to minimize risk to the nerve as the remaining components, including parts II and III, subsequently dissolve in a sequential fashion determined by the kinetics of dissolution, starting with the residual Mg, followed by the Mo/PLGA, and finally by the C-wax. Figure 1 (D and E) shows this process through photographs captured at various elapsed times following immersion in 1× PBS (pH 7.4) at physiological temperature (37°C). The PA-encapsulated Mg (extension electrodes) in parts I and II dissolves first within 10 days (Fig. 1D), while the C-wax (electrical connection) and the Mo/PLGA (nerve cuff) in parts II and III remain. The use of PA100 (with the highest permeation and dissolution properties among the PAs demonstrated in this work) in Fig. 1D leads to degradation of Mg electrodes within days. This period, relative to the functional lifetime of the cuff electrode, can be tuned from several weeks to months, depending on the type of PA. Complete degradation of the PA and PLGA occurs over a period of months, depending on the formulations. The wax reported here is biodegradable and biocompatible, with a degradation rate of ~10 μm per month in vivo (*32*, *33*). In the absence of electrochemical mechanisms associated with stimulation, the Mo electrodes gradually disintegrate into small fragments within 2 months (Fig. 1E) and then fully disappear at a rate of 0.02 μm/day (*31*).

The kinetics of the processes of dissolution of the encapsulated regions of metal and the various structural elements of the device can be influenced by the chemistry of the constituent polymers. For

example, the ratio of lactide to glycolide in the PLGA [i.e., 75:25, 65:35, and 50:50 (lactide:glycolide)] determines the lifetime of the cuff (*41*). The use of a 50:50 ratio causes the cuff to unfurl and release from the nerve more quickly than the others due to its relatively high rate of dissolution (*42*), resulting in rapid disruption (within 2 weeks) of a tubular shape during immersion in 1× PBS (pH 7.4; 37°C) (fig. S8). By contrast, the 75:25 version maintains the original shape for more than 4 weeks under similar conditions. The chemistry of the PA-based encapsulant influences the permeation of biofluids and dissolution kinetics. The formulation used here consists of two types of PAs with different permeation and dissolution rates, as described subsequently.

Electrical stimulation capabilities

Reliable pain block requires the application of KHFAC (10 V_{pp}, 25 kHz) at the neural interface for time periods that address the clinical need, where durations of each stimulation event can reach several minutes to hours per day (*30*). As described in previous studies with nonresorbable devices, recovery of nerve conduction occurs immediately after cessation of short periods of blocking stimulation (*19*, *21*). By contrast, stimulation for tens of minutes or hours leads to slow recovery due to carryover effects (*19*, *43*).

Metal-based electrodes may corrode spontaneously in contact with the biological electrolyte under electrical stimulation, by either uniform or grain-selective attack (*44*). Electrochemical characterization [e.g., electrochemical impedance spectroscopy (EIS) and cyclic voltammetry (CV)] for the Mo reveals aspects related to the efficiency and electrochemical safety of stimulation. Platinum (Pt) serves as a relevant comparison, selected because of its use in conventional devices for nerve conduction block and its favorable combination of electrical conductivity (4.4×10^6 S/m at 37°C), charge storage capacity and charge injection capacity (CSC and CIC; the maximum deliverable charge per unit area, ~5 and 0.83 mC/cm^2), biocompatibility, and corrosion resistance (*45*–*47*). Figure 2A shows Bode plots over a frequency range of 1 to 10^5 Hz for electrodes of Mo (15 μm thick) and bare Pt (12.5 μm thick), both with the same exposed areas (0.3×10 mm^2) to 1× PBS (pH 7.4; 37°C). The impedance of Mo is slightly higher than that of Pt at low frequencies (1 to 10^3 Hz), but the values are nearly identical at frequencies (10^3 to 10^5 Hz) relevant to KHFAC (Fig. 2A). For 10^3 to 10^5 Hz, the slopes of impedance spectra are both close to 0 and the phase angles approach 0°, indicating that Mo and Pt electrodes represent similar ionic resistances to PBS [i.e., comparable solution resistance (R_s)] (fig. S9A) (*48*, *49*).

Comparisons of the stimulation capability between the Mo and Pt electrodes follow from the results of electrical stimulation (input: AC, frequency of 25 kHz, amplitude of 10 V_{pp}) applied in 1× PBS (pH 7.4; 37°C) for 1 hour (Fig. 2B). Both electrodes exhibit stable output waveforms at 25 kHz (Fig. 2C). Figure 2D shows the results of surface characterization of the Mo electrode before and after this test. The roughness (arithmetical mean height, S_a) increases (from 0.077 to 0.559 μm) due to electrochemically accelerated surface corrosion (*50*, *51*).

Multiple cycles of this type of electrical stimulation are essential to envisioned uses in pain mitigation. Studies of the stability of Mo electrodes in such scenarios involve single electrical stimulation (AC, 25 kHz, 10 V_{pp}, 1 hour) in 1× PBS (pH 7.4) at body temperature across multiple episodes each day for 2 weeks (i.e., 14 times in total number) (Fig. 2, E to I). Comparisons are to a control group defined by Mo electrodes immersed in 1× PBS (pH 7.4; 37°C) for 2 weeks without electrical stimulation. The highest impedance occurs on week 0, with values that decrease with increasing stimulation (Fig. 2, E and F). The phase angles remain at 0° over a wide range of frequencies and shift toward lower frequencies with time, consistent with the progression of electrochemical corrosion (*52*). Similar trends occur with reduced magnitudes in the control group, as a result of comparatively slow rates of natural corrosion of the metal (fig. S10).

Scanning electron microscopy (SEM) images provide insights into changes in surface morphology associated with electrical stimulation that can explain, at least in part, these behaviors (Fig. 2G, top, and figs. S10 and S11). As the total time of stimulation increases, the Mo surface exhibits increasing densities of irregular, microscale channeling cracks (*48*, *52*). These morphological features increase the effective surface areas, and they allow diffusion of the electrolyte (i.e., 1× PBS) into the resulting interfaces to the underlying metal (i.e., Mo) surfaces, as the origins of the decreasing R_s value in Nyquist plots (fig. S9, C to E). Such diffusion processes, allowing facile charge transfer, contribute to the ability of the Mo electrode to deliver electrical stimulation throughout the period of immersion (Fig. 2G, bottom, and fig. S11).

These changes can also affect the CSC, as another metric relevant to stimulation. Figure 2H shows CV curves for each electrode collected by sweeping the applied voltage from −0.6 to 0.0 V at a scan rate of 50 mV/s. For cathodic CSC (CSC_c), the following equation can be used: CSC_c (C/cm^2) = $\int_{E_c}^{E_a} |i| dE/\nu A$, where E is the potential (V versus reference electrode); i is the cathodic current (A), E_a and E_c are the anodic and cathodic potential limit (V), respectively; A is the geometric surface area of the exposed electrode (cm^2; here, we used a projection area of 300 μm wide × 10 mm long); and ν is the scan rate (*46*). The numerator in this equation corresponds to the colored area of the CV curves. CSC_c increases after 2 weeks of multiple stimulation in 1× PBS (pH 7.4; 37°C) according to parameters described previously, due to the electrochemically grown oxide layer on the Mo surface (week 0: 0.4 mC/cm^2; week 1: 19 mC/cm^2; week 2: 40 mC/cm^2) (Fig. 2I). Likewise, CIC is an important factor in evaluating the electrical stimulation performance of the electrodes over time. The CIC value of the Mo electrode on week 0 (0.7 mC/cm^2 for a 0.5-ms pulse) is comparable to those of traditional stimulating electrodes (e.g., Pt: 0.8 mC/cm^2, Au: 0.2 mC/cm^2, and TiN: 0.9 mC/cm^2 for >0.5-ms pulses) (*45*, *53*). Furthermore, the CIC value slightly increases after 2 weeks of multiple stimulation (once per each day; AC, 25 kHz, 10 V_{pp}, 1 hour) in 1 × PBS (pH 7.4; 37°C), following the behavior of CSC_c (week 0: 0.7 mC/cm^2; week 1: 1.2 mC/cm^2; week 2: 1.7 mC/cm^2; fig. S12).

These results indicate that Mo electrodes can provide consistent nerve block performance across a relevant therapeutic period, as a stimulating electrode. In general, charge transfer across the electrode-tissue interface can be achieved by electrostatic adsorption/desorption of ions in electrolytes (non-Faradaic, capacitive) or reduction/oxidation of surface-confined chemical species (Faradaic, pseudocapacitive). The grown oxide layer and associated networks of microcracks contribute to the pseudocapacitive behavior and the morphological changes of the Mo electrode, thereby increasing the CSC values and decreasing the impedance values, respectively. Overall, the equivalent electrical circuit model and fitted results can capture the trends in the EIS data for the stimulated Mo electrode (fig. S9, B to E). In this model, changes in electrochemical parameters (resistance of electrolyte, R_s; corrosion resistance of oxide film, R_f; capacitance of oxide film, C_f; charge-transfer resistance

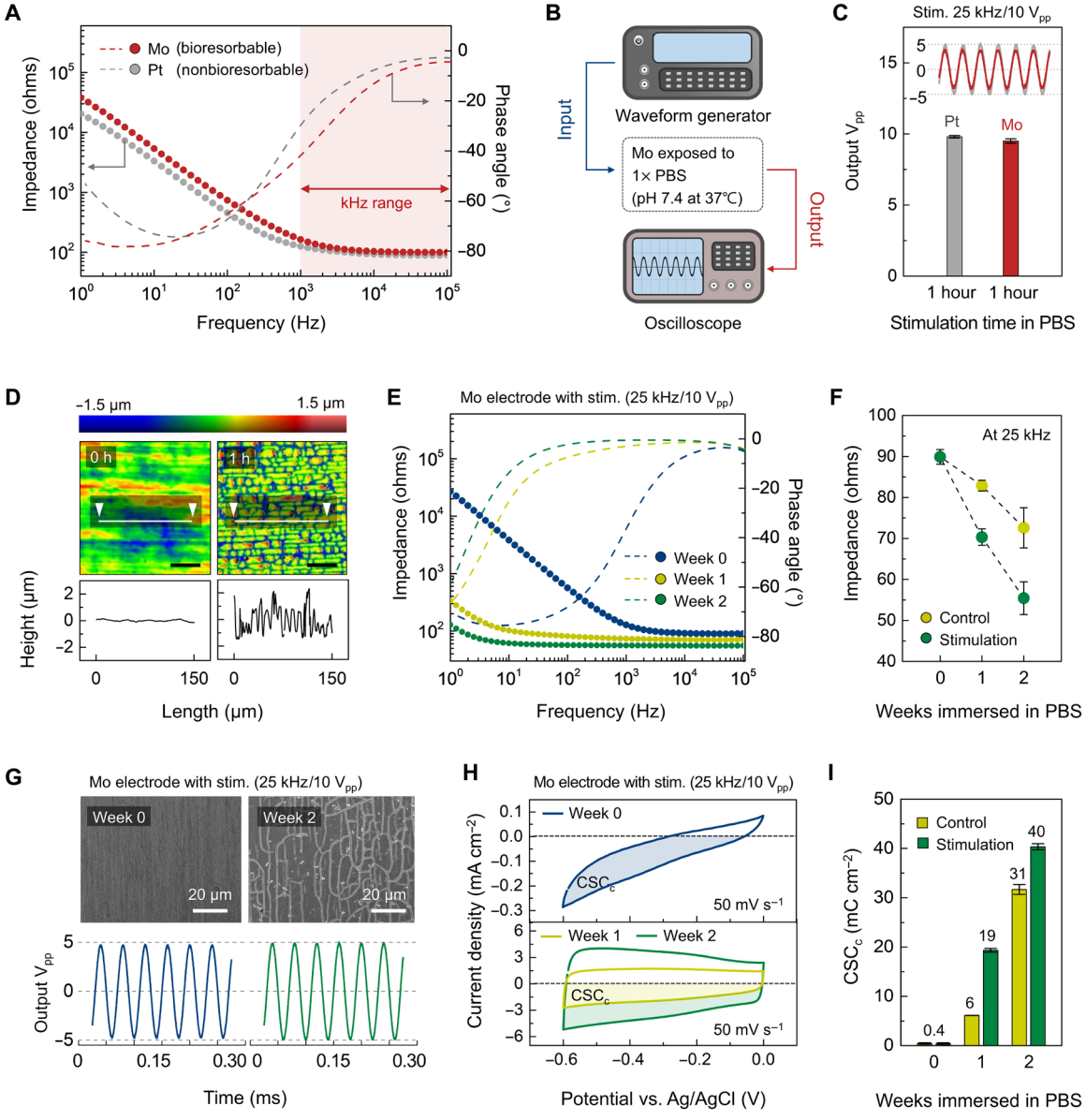

Fig. 2. Electrochemical and morphological properties of bioresorbable electrodes under physiological conditions. (**A**) Bode plots of Pt and Mo electrodes. Here, the dotted and dashed lines represent the impedance magnitude and the phase angle, respectively. (**B**) Diagram of the experimental setup for controlling input electrical waveforms and monitoring output waveforms associated with electrodes immersed in PBS under physiological conditions. (**C**) Changes in output V_{pp} supplied by Pt and Mo electrodes. KHFAC continuously applied to each electrode for 1 hour defined the input stimulation conditions. Inset: Output waveforms after stimulation for 1 hour. (**D**) Surface topography of a Mo electrode before and after electrical stimulation. Scan area, 150 µm × 150 µm. (**E**) Bode plots of a Mo electrode under electrical stimulation across multiple episodes. (**F**) Changes in impedance magnitude for control and stimulation Mo electrodes at weeks 0, 1, and 2 at a frequency of 25 kHz. (**G**) SEM images (top) of a Mo electrode under electrical stimulation across multiple episodes for 2 weeks and corresponding output waveform (bottom). Scale bars, 20 µm. (**H**) CV curves of a Mo electrode under electrical stimulation across multiple episodes for 2 weeks. Colored area was used for the calculation of CSC_c. (**I**) Changes in CSC_c for control and stimulation Mo electrodes at weeks 0, 1, and 2 at a scan rate of 50 mV/s. In (D) to (I), physiological conditions, 1× PBS (pH 7.4; 37°C). Electrical stimulation, once per each day; AC, 25 kHz, 10 V_{pp}, 1 hour. Independent experiments and samples, $n = 4$. All error bars, SD.

of the corrosion process, R_{ct}) confirm the electrochemical processes at the metal electrode/electrolyte interface during chronic electrical stimulation (once per each day; AC, 25 kHz, 10 V_{pp}, 1 hour), decreasing R_s, R_f, and R_{ct} and increasing C_f, as evidence of corrosion (*48*). By comparison, Pt electrodes exhibit invariant electrochemical performance over this same 2-week time period, with or without electrical stimulation, due to their corrosion resistance (fig. S13).

Results related to the long-term (up to 4 weeks) electrochemical performance of Mo electrodes are in fig. S10. Under electrical stimulation (once per each day; AC, 25 kHz, 10 V_{pp}, 1 hour), Mo electrodes immersed in 1× PBS (pH 7.4; 37°C) show similar trends (i.e., decreasing impedance and increasing CSC_c) to those obtained over 2 weeks. Overall, the multiple stimulation group achieves marked changes in impedance, CSC_c, CIC and surface morphology, compared to the control group, consistent with the effects of electrical stimulation

on corrosive processes (*48*, *50*–*52*). These systematic electrochemical studies demonstrate that Mo can deliver reliable electrical stimulation required for nerve block, serving as a bioresorbable alternative to Pt.

Permeation and dissolution properties of an encapsulant

The encapsulation materials for the extension electrodes and their interface through the woven structure define the time scales for mechanical/electrical decoupling. The encapsulation used here exploits two different bioresorbable forms of PA, as shown in Fig. 3A, consisting of polybuthanedithiol 1,3,5-triallyl-1,3,5-triazine-2,4,6(1*H*,3*H*,5*H*)-trione pentenoic anhydride (PBTPA; type I) (*38*) and poly(ethylene glycol) diacrylate pentenoic anhydride (PEGPA; type II) (*40*). Both chemistries contain 4-pentenoic anhydride (4PA) as locations for chain scission by hydrolysis. The use of a hydrophobic crosslinker, 1,4-butanedithiol (BDT), to form polymeric chains with 4PA yields low water permeability, thereby also reducing the rate of hydrolysis of the PBTPA (~1.3 μm/day) under physiological conditions [1× PBS (pH 7.4), 37°C] (*38*). The rates for PEGPA (~27 μm/day) are higher than those for PBTPA and its hydrophilic crosslinker [i.e., poly(ethylene glycol) diacrylate (PEGDA)] (*40*). Simple mixing of these two PAs in solution yields polymer blends that offer the desired water permeability and rate of hydrolysis. Liquid mixtures of PBTPA and PEGPA in solutions that consist of anhydride monomer, allyl group containing monomer, crosslinker, and photoinitiator, can be crosslinked via thiol-ene photopolymerization, starting with exposure to ultraviolet (UV) light. The synthesis procedures appear in Materials and Methods and fig. S14 (A and B) (*38*, *40*). Results presented here focus on four types of polymers (PA100, PA80, PA65, and PA50) with different relative ratios of PEGDA (fig. S14C).

Figure 3B shows the time-dependent changes in the resistances of Mg electrodes (1 mm wide, 15 μm thick) encapsulated with four types of PA (20 mm wide, 20 mm long, 400 μm thick) after exposure (exposed area, 1 × 10 mm^2) to 1× PBS, pH 7.4, at 37°C. Structures with films of PA50 and PA65 maintain their electrical conductivity for longer durations (30 days) compared to those with films of PA100 (6 days) and PA80 (10 days) due to different water-barrier properties, consistent with their relative rates of dissolution. The findings illustrate the ability to adjust the electrical lifetime through choices in PA chemistry. The use of PA50 leads to stable electrical performance (10 ohms or less) in the woven electrode (Mo/Mg coated with C-wax) for more than 30 days (fig. S15).

Figure 3C shows the dissolution behavior (i.e., hydrolysis) of the encapsulant. As the films absorb water, hydrolysis of an anhydride

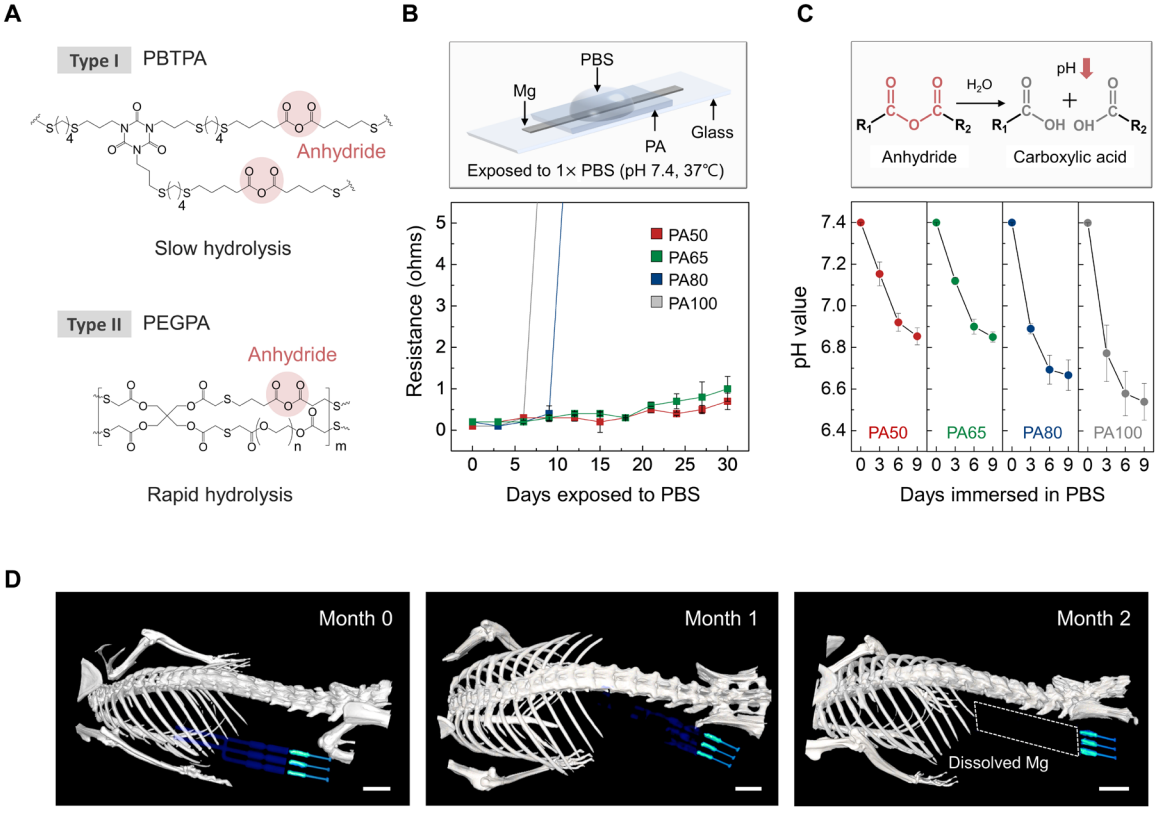

Fig. 3. Dissolution characteristics of an encapsulant studied in vitro and of a complete system studied in vivo. (**A**) Chemical structure of the major components of the PA encapsulant. Synthesis occurs by photopolymerization of a liquid mixture of chemical precursors. Type I (PBTPA) and type II (PEGPA) have low and high rates of bioresorption, respectively, due to the hydrolysis of anhydride groups. (**B**) Changes in resistance of a Mg electrode (1 mm wide, 10 mm long, 50 μm thick) encapsulated with PA films with different formulations as a function of immersion time in 1× PBS (pH 7.4; 37°C). Independent samples, $n = 4$. Error bars, SD. (**C**) Time-dependent changes in pH of the PA films (5 mm wide, 5 mm long, 400 μm thick, 20 mg weight) during immersion in 1× PBS (pH 7.4; 37°C). Inset: Hydrolysis reaction of an anhydride group into two carboxylic acid groups. Independent samples, $n = 4$. Error bars, SD. (**D**) Three-dimensionally rendered CT images of mice collected over 2 months after implantation of a bioresorbable nerve stimulator. The images indicate the gradual disappearance of the Mg electrodes until they are no longer visible on month 2. Scale bars, 5 mm. Biologically independent mice, $n = 4$.

group produces two carboxylic acid groups, leading to a change in the pH of the surrounding environment (*40*). Mixed films (5 mm wide, 5 mm long, 400 μm thick, 20 mg weight) with four different ratios of PEGDA immersed in 1× PBS (pH 7.4; 37°C) show different rates of change in pH due to this reaction. These data indicate that the PA100 film degrades faster than the others, and in all cases, no changes appear after 9 days. Films of pure PEGPA (nonmixed) undergo rapid dissolution in PBS, with large changes in pH (fig. S16).

Computed x-ray tomography (CT) images provide additional insights into the dissolution processes for devices encapsulated with PA50 (Fig. 3D). Thin films of high-radiocontrast metal (W, ~700 nm thick) coated onto the extension electrodes (Mg, 50 μm thick) enhance visibility in the CT images (*41*). The results show a steady and sequential disappearance of devices implanted in the subcutaneous region in the hind leg as the PA dissolves. Throughout month 0, the entire device, including parts I, II, and III, is clearly visible. In month 1, the Mg/W electrodes in parts I and II begin to dissolve. The Mg/W electrodes completely disappear in month 2, while the Mo electrodes and the C-wax in parts II and III remain visible (images of extracted devices are in fig. S17). These sequential bioresorption behaviors are consistent with observations in vitro, described previously (Fig. 1D).

The thin, flexible structures explored here (8 mm wide, 20 mm long, 400 μm thick) are favorable for interfaces to soft nerve tissues. The Young's modulus for the PA lies between 4.4 and 6.0 MPa (PA100, 6.0 MPa; PA80, 5.6 MPa; PA65, 5.0 MPa; PA50, 4.4 MPa; fig. S18). As the molar ratio of 4PA decreases and that of PEGDA increases (from PA100 to PA50), the elongation of the film improves and Young's modulus decreases. Furthermore, durability tests with the PA-encapsulated woven electrode indicate stable operation during compression-induced bending [ranging from 0 to 50%; calculated as $(l - l_0)/l_0 \times 100$ (%)] and under cyclic loading (compression to 30%; involving buckling: 5 mm/s rate, 2000 cycles) (fig. S4A). The resistance of the woven electrode remains unchanged even under extreme deformations (i.e., twisting with 45° to 270°; repetitive twisting cycle of 180°, 30°/s rate, 2000 cycles) (fig. S4B). These results suggest a level of robustness in operation necessary for use in vivo in freely moving animals (*41*, *54*).

In vivo demonstrations of nerve conduction block

Investigations of nerve conduction block in rat models illustrate capabilities for reversible block of evoked neural signals. Acute animal tests involve a dorsolateral gluteal muscle–splitting incision to allow insertion of three separate electrodes: a stimulating electrode that wraps the proximal sciatic nerve to induce an action potential that propagates along the nerve, a blocking electrode that wraps the nerve at a location distal to the stimulating electrode to deliver a KHFAC waveform that arrests and prevents continued propagation of the action potential, and a recording electrode that wraps the peroneal nerve at a position distal to both the stimulating and blocking electrodes, to detect the presence/absence of neural activity (Fig. 4A). This configuration of electrodes (i.e., proximal stimulating and distal recording) follows other procedures for nerve assessments, including previous studies on nerve conduction block using a related mechanism (*19*, *55*). Measurements performed by switching the electrode positions (i.e., distal stimulating and proximal recording) show physiologically similar results due to the bidirectionality of action potential propagation in peripheral nerves with exogenous electrical stimulation (fig. S19) (*56*, *57*).

Cross-sectional images of the sciatic nerve collected before and after KHFAC stimulation (25 kHz, 10 V_{pp}, 1 hour) for complete nerve block, as described below, reveal no signs of axonal damage (Fig. 4B). Methods for examining the efficacy of this block rely on recordings of compound nerve action potential (CNAP; for sensory and motor block) and measurements of muscle force (for motor block) (*6*). The former is a direct method to observe the block, and the latter represents the effect on the relevant motor fibers. Varying the parameters [i.e., frequency (Hz) and amplitude (V_{pp})] of the KHFAC waveform defines optimal conditions. Figure 4C shows the changes in CNAP depending on these parameters. These data indicate complete sensory block under two conditions: (i) KHFAC of 8 and 10 V_{pp} at a frequency of 25 kHz or (ii) KHFAC of 25 and 35 kHz with an amplitude of 10 V_{pp}, consistent with previous reports based on nonresorbable devices (*6*, *19*, *21*). Muscle force experiments help to quantify the extent of the motor block. Input waveforms at frequencies of 25 kHz and with amplitudes above 6 V_{pp} yield no muscle twitches upon stimulation (Fig. 4D), consistent with the CNAP recordings.

Studies of devices constructed for multiday testing involve implantable nerve cuffs mounted to the nerves for stimulating (nonbioresorbable), blocking (bioresorbable device under test), and recording (nonbioresorbable). Wired connections route subcutaneously along the spine to a headcap (Fig. 4E). The stimulating cuff includes bipolar electrodes (Pt; 300 μm wide, 12.5 μm thick, 1 mm interspacing); the bioresorbable blocking cuff incorporates tripolar electrodes (Mo; 300 μm wide, 15 μm thick, 1 mm interspacing); and the recording cuff is composed of bipolar electrodes (Pt; 100 μm wide, 15 μm thick, 1 mm interspacing). Details associated with the electrodes and the surgical procedures for implantation are in figs. S20 and S21. CNAP and muscle force measurements in a live animal model indicate consistent blocking performance across a relevant therapeutic period (Fig. 4F), corresponding to 9 days after implantation.

Studies of biocompatibility

Biocompatibility of the constituent materials for these devices and of the products of their bioresorption is extremely important. The key components (Mg and Mo as an electrode; PLGA as a nerve cuff; C-wax as a conductive paste; PA as an encapsulant/substrate) yield end products that can be further metabolized and resorbed by the body (*31*, *33*, *38*–*40*, *58*). Information on foreign body reactions can be obtained by subcutaneously implanting devices into an experimental group of animals and pieces of high-density polyethylene (HDPE; a U.S. Food and Drug Administration–approved biocompatible material; 10 μm thick) into a control group. The results in Fig. 5 (A and B) indicate that changes in body and organ weight for mice in these two groups share similar trends throughout the period of observation. The mice behave normally without any skin necrosis or swelling for 8 weeks after implantation. Figure 5B shows minimal changes in the weight of key organs explanted at 2, 4, 6, and 8 weeks after implantation (only 8 weeks for the control group). Given that Mg and PA fully dissolve within weeks, this result indicates an absence of toxic effects.

For histological analysis, hematoxylin and eosin (H&E)–stained sections of implant sites, surrounding tissues, and major organs (brain, liver, kidney, spleen, lung, and heart) show no discernible immune reactions related to implantation such as oxidative damage to cellular lipids, inhibition of mitochondrial activity, or hyperplasia of macrophages due to excessive absorption of metal ions (Fig. 5C). Moreover,

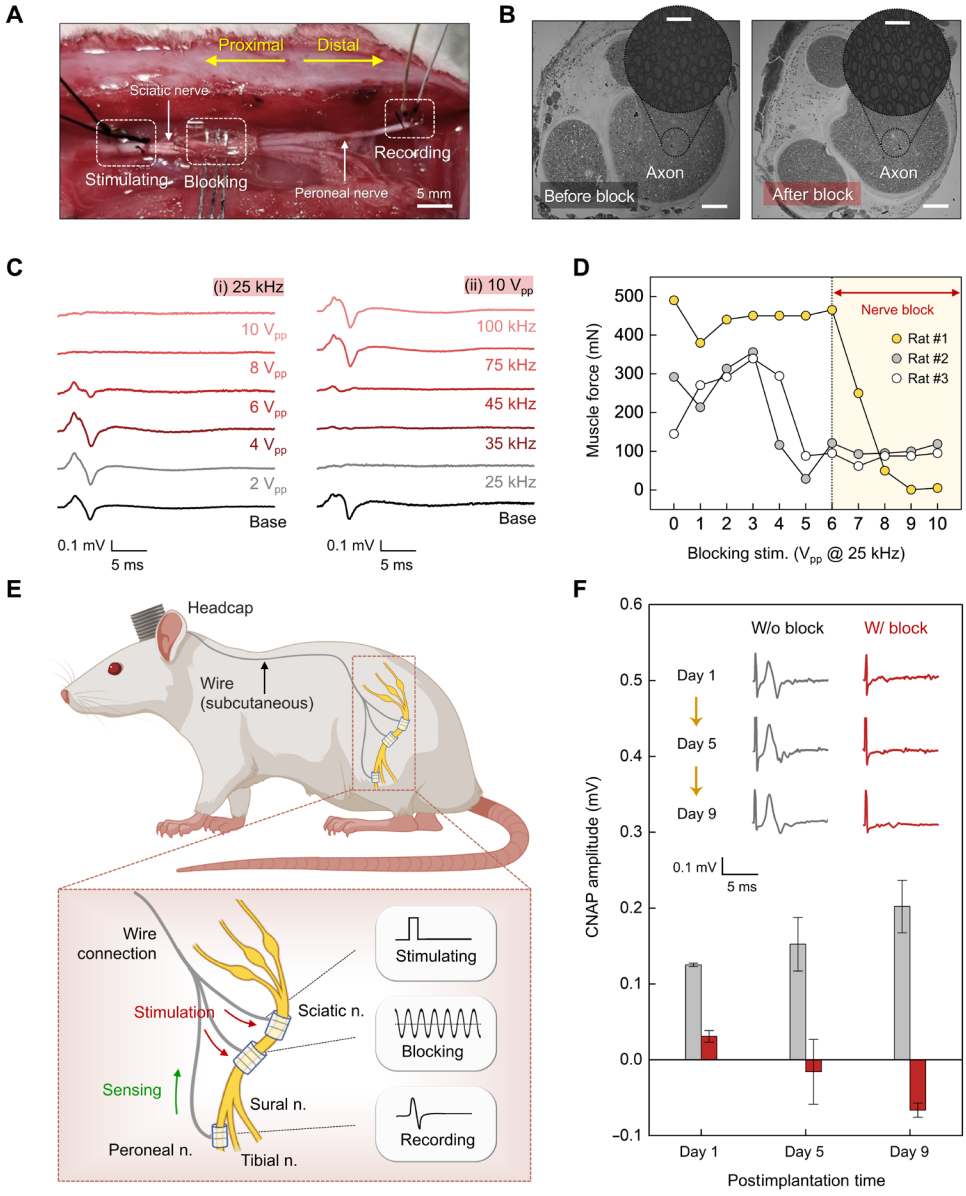

Fig. 4. In vivo tests for KHFAC nerve conduction block with a bioresorbable electrical stimulator. (**A**) Experimental arrangement of electrodes for acute in vivo electrophysiology studies. The setup consists of three types of electrodes: (i) a stimulating electrode placed on the sciatic nerve for proximal stimulation, (ii) a blocking electrode placed between the stimulating and recording electrodes for conduction block using KHFAC, and (iii) a recording electrode placed on the peroneal nerve for recording CNAP amplitude. Scale bar, 5 mm. (**B**) Cross-sectional images of the sciatic nerve before (left) and after (right) electrical stimulation (AC, 25 kHz, 10 V_{pp}). Scale bars, 200 μm. Inset: Magnified images of each axon. Scale bars, 50 μm. Independent samples, $n = 4$. (**C**) Block effectiveness for various KHFAC stimulation parameters. (i) Effect of block amplitude (2, 4, 6, 8, and 10 V_{pp}) on CNAP recordings at a frequency of 25 kHz. (ii) Effect of block frequency (25, 35, 45, 75, and 100 kHz) on CNAP recordings at an amplitude of 10 V_{pp}. (**D**) Effect on muscle force from various amplitudes of blocking stimulation at a frequency of 25 kHz. (**E**) Illustration for implanting the device. Top: Subcutaneous routing path of the nerve cuffs and wire interconnects. Bottom: Stimulating, blocking, and recording cuffs wrapped around nerves. (**F**) Changes in CNAP amplitudes under stimulation for nerve conduction block for 9 days. Inset: Representative CNAP trace elicited by the optimized electrical stimulation (AC, 25 kHz, 10 V_{pp}) of the corresponding day. In (C) to (F), independent devices ($n = 3$) in biologically independent rats ($n = 3$) with similar results. All error bars, SD.

fibrous capsules around the implants as quantified by H&E image analysis at week 8 present no significant differences between the control and device-implanted group with capsular thicknesses of 36 ± 3 and 39 ± 5 μm, respectively (Fig. 5D).

In addition, histological analysis focusing on the sciatic nerve at three time points (months 1, 3, and 6) after device implantation reveals that the device does not harm the surrounding sciatic nerve and muscle fibers. Transverse images from the sciatic nerve in Fig. 5E exhibit healthy and myelinated axons in nerve fascicles during 6 months of in vivo studies without vacuolation, which is an indicator of a chronic inflammatory response. Figure 5F indicates healthy cells within the gastrocnemius muscles at 1, 3, and 6 months. In addition, inflammation-related reactions including collagen hyperplasia and atrophied muscle fibers are absent (*59*, *60*). The cross-sectional

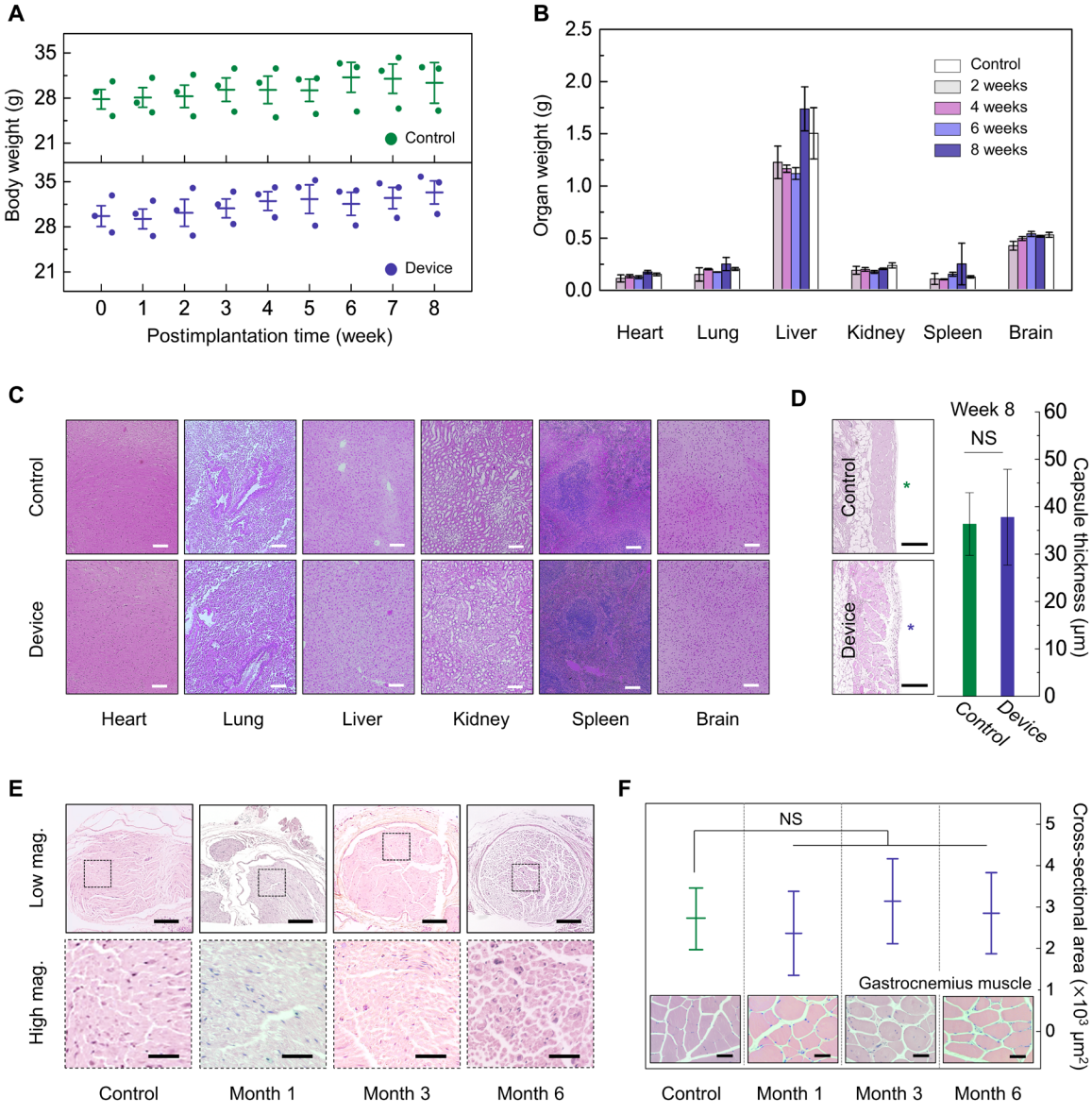

Fig. 5. Biocompatibility studies of a bioresorbable nerve stimulator. (**A**) Changes in body weight for control (HDPE) and experimental (bioresorbable device) groups measured weekly for 8 weeks. (**B**) Changes in organ (heart, lung, liver, kidney, spleen, and brain) weight in each group at 2, 4, 6, and 8 weeks. (**C**) Histology images of the heart, lung, liver, kidney, spleen, and brain tissues stained with H&E of the control and experimental groups implanted for 8 weeks. Scale bars, 200 μm. (**D**) Images and thicknesses of fibrous capsules around implants at week 8. The thicknesses correspond to values obtained by image analysis. Star symbols, sites of implantation. Scale bars, 500 μm. (**E**) Histological analysis (H&E-stained sections) through the interface between the nerve cuff and the sciatic nerve for 1, 3, and 6 months after implantation (top) and zoomed images (bottom). Axons shown in the transverse sections indicate no sign of chronic inflammation or local toxicity. Scale bars, 300 μm (top) and 50 μm (bottom). (**F**) Quantitative analysis through a cross-sectional area of gastrocnemius muscle fibers for 1, 3, and 6 months after implantation. Inset: Cross-sectional images of gastrocnemius muscle. Scale bars, 50 μm. In (A) to (F), implantation was in the subcutaneous region near the right hind leg. Biologically independent mice (A to D) and rats (E and F): control group, $n = 3$; experimental group, $n = 3$. All error bars, SD. P values of >0.05, no statistical significance. NS, not significant.

areas of the muscle fibers show no statistically significant differences across all groups (Fig. 5F, inset).

DISCUSSION

Engineering schemes for pain management may provide powerful alternatives or complements to traditional pharmacological approaches. The work presented here establishes classes of devices that allow electrically precise, reversible blocking of peripheral nerve activity in living animal models. The material compositions, design choices, and fabrication approaches yield thin, flexible form factors and fully bioresorbable characteristics to bypass many of the intrinsic disadvantages of previous technologies for certain use cases. Detailed studies define a set of engineering principles for reliable, biocompatible operation tailored to clinical requirements in therapeutic timelines. Direct, conformal contact to the nerve enables rapid, repeatable, and reversible pain block. A key feature is in a multicomponent, multimaterial architecture that supports time-sequential bioresorption mechanisms to allow electrical

and mechanical decoupling from the nerve in a manner that minimizes the potential for damage to soft tissues after a desired operating period. These processes also bypass the need for secondary surgical extraction procedures. Future opportunities include the use of stimuli-responsive materials for triggered degradation, the development of leadless, miniaturized systems with fully wireless operation, and the integration of sensing modalities for closed-loop control.

MATERIALS AND METHODS

Preparation of bioresorbable peripheral nerve stimulators

Woven electrodes

Laser-cut strips of Mg (50 μm thick; GoodFellow) and Mo (15 μm thick; GoodFellow) formed interconnections and cuff electrodes, respectively. Inserting the sharp ends of the Mo strips in an alternating fashion into slits formed in the Mg strips yielded a mechanically woven connection. An electrically conductive paste consisting of W microparticles (5 μm in particle size; Sigma-Aldrich) in a matrix of candelilla wax (Sigma-Aldrich) coated the woven connections to improve the electrical and mechanical properties of the interface.

Encapsulants and substrates

Crosslinking a mixture of PBTPA (slow hydrolysis) and PEGPA (rapid hydrolysis) precursors yielded materials for free-standing substrates to support the active and encapsulant elements of the devices to prevent direct contact with the surrounding biofluids. For preparation of PBTPA, chemical precursors of 4PA, 1,3,5-triallyl-1,3,5-triazine-2,4,6(1*H*,3*H*,5*H*)-trione (TTT), and BDT were mixed in a molar ratio of 1:4:7. Similarly, 4PA, PEGDA (average M_n of 575), and pentaerythritol tetrakis(mercaptoacetate) were prepared for PEGPA. Control of the molar ratio of the precursors for PEGDA influenced the crosslinking density and the hydrolysis rate. For instance, with PA50, the synthesis began with 1.0 g of PEGDA (0, 0.4, and 0.7 g for PA100, PA80, and PA65, respectively) and 1.7 g of pentaerythritol tetrakis(mercaptoacetate), followed by mixing equal volumes of PBTPA solution. The addition of 2,2-dimethoxy-2-phenylacetophenone (30 mg) as a photoinitiator enabled photopolymerization under illumination with UV light (365 nm in wavelength, 590 μW/cm^2 in intensity) for 5 min. A summary of the mass appears in fig. S14C. All chemicals from Sigma-Aldrich were used as purchased, without further purification.

Assembly

The woven electrodes were placed on the partially cured, tacky surface of the PA substrate. Coatings of uncured PA ensured strong adhesion of the films of PA to themselves to form a top encapsulating layer. Exposure to UV light (365 nm in wavelength, 590 μW/cm^2 in intensity) for 5 min led to additional crosslinking between the layers to yield the final device.

Materials characterization

Electrochemical characterization

An electrochemical analyzer (Autolab, Metrohm) using a three-electrode cell recorded the electrochemical behavior of Mo and Pt electrodes in 1× PBS (pH 7.4; 37°C) as a function of immersion time. The reference, counter, and working electrodes consisted of a Ag/AgCl electrode (3 M KCl; BASi), a wire of Pt (0.5 mm in diameter), and strips of Mo (300 μm wide, 10 mm long, 15 μm thick) and Pt (300 μm wide, 10 mm long, 12.5 μm thick), respectively. EIS used an AC perturbation amplitude of 10 mV across a frequency range of 1 to 10^5 Hz. CV was performed with a potential from −0.6 to 0.0 V versus a Ag/AgCl electrode and at a scan rate of 50 mV/s. From the collected voltammograms, CSC_c was calculated for each electrode. Voltage transients captured under chronopotentiometry mode revealed behaviors associated with various injected biphasic, cathodal first, symmetric current pulses (pulse width, 500 μs; interpulse delay, 10 μs). Practically, the measurements began from a low current amplitude (i.e., 1 mA), followed by a stepwise increase in the current until the cathodic polarization (E_{mc}) reached the water reduction limit (−0.6 V). E_{mc} corresponds to the electrode potential versus the reference electrode evaluated 10 μs after the cathodal pulses. The CIC_{max} follows from multiplication of the current amplitude and pulse width divided by the surface area (300 μm wide, 10 mm long).

Morphological characterization

Images obtained with a SEM (Hitachi S-4800, Hitachi High-Technologies Corporation) captured the morphology of the surfaces of electrochemically corrosive Mo electrodes. Thin Pt coatings enhanced the clarity of images obtained at an applied voltage of 10 kV and working distance of 9.6 mm in both low- and high-resolution modes. For additional characterization of the surface topography, a three-dimensional optical profiler (Zygo Corporation) recorded images of the surface roughness of the Mo electrodes after immersion in 1× PBS (pH 7.4; 37°C) for 2 weeks. Images of electrodes were obtained after applying an AC signal (25 kHz, 10 V_{pp}) for various times (5, 30, and 60 min) each day during immersion in 1× PBS (pH 7.4; 37°C).

Mechanical characterization

Dynamic mechanical analysis (RSA-G2 solid analyzer) used test samples of PA100, PA80, PA65, and PA50 (8 mm wide, 20 mm long, 400 μm thick) to measure the tensile stress as a function of strain. Measurements of mechanical forces required to disconnect (Mark-10 force gauge, MARK-10) confirmed the durability of the woven electrode (interleaved connection) in comparison with the control electrode (end-to-end connection). Durability tests of the woven electrode involved repetitive mechanical cycling (bending and twisting). Uniaxial compression and rotation with speeds of 5 mm/s and 30°/s, respectively, caused buckling and twisting for each woven electrode at room temperature.

Tests for dissolution and water permeability

Placing polydimethylsiloxane well structures (15 mm × 15 mm outer, 9 mm × 9 mm inner, 1 cm deep) on laser-cut pieces of metal foils (Mg, 50 μm thick; Mo, 15 μm thick) or on PA-encapsulated electrodes and filling them with 1× PBS (pH 7.4; 37°C) provided platforms to test the dissolution of the metals and the water permeability of the encapsulants. The PBS in each well was refreshed on a daily basis.

Surgical procedures for device implantation

Preparation of surgery

Surgical procedures began with anesthetizing the rats with 5% isoflurane/95% oxygen (induction) and 2% isoflurane/98% oxygen (maintenance), administered via inhalation. Preparation of the animals involved shaving the fur, applying isopropanol and Betadine to the right leg, and introducing analgesia through a subcutaneous injection of Buprenorphine SR (1 mg/ml; ZooPharm) with a dose of 1.2 mg/kg. The surgery began with an incision parallel to the right femur to split the gluteal muscles and the biceps femoris. Blunt dissection mobilized the sciatic nerve and the peroneal branch. The nerve cuffs were connected to a female Omnetics connector (part no. A79044-001, Omnetics Connector Corporation). PLGA-based cuffs wrapped

circumferentially around the sciatic nerve. The bipolar stimulating cuff was located 5 mm proximal to the tripolar blocking cuff. The recording cuff (custom order, MicroProbes) was placed 5 mm distal from the blocking cuff around the peroneal branch. Femoral muscle layers and skin were sutured with Vicryl 5-0 suture (Ethicon) and Nylon 4-0 suture (McKesson Medical-Surgical) to close the incision.

Headcap connection

A sagittal incision exposed the skull, which was subsequently cleaned of tissue using a scalpel, cotton-tipped applicators, gauze, hydrogen peroxide, and acetone. Blunt dissection opened a subcutaneous pocket from the sciatic nerve to the skull. A titanium chamber, henceforth referred to as the headcap, placed on the skull served as an interface point for routed wires through the subcutaneous pocket. Four screws drilled into the skull secured the headcap to the skull. Dental acrylic (Joyfil, 3D Dental) further fixed the system to the skull. A 4-0 nylon suture closed the skin.

Electrophysiology measurements

CNAP tests

The block stimuli were provided by a waveform generator (Agilent, 33250A) producing biphasic, charge-balanced, sinusoidal waveforms with various peak-to-peak voltages (from 2 to 10 V_{pp}) and frequencies (from 25 to 100 kHz). After 15 s, a custom stimulation system and data acquisition software (Red Rock Laboratories) generated stimulation pulses (amplitude, 1 mV; burst width, 0.3 s; duration, 50 μs), and the resulting CNAP signal was amplified and recorded. The lack or presence of a twitch response due to the stimulation pulse before deactivating the block was observed. For testing of the implants, the male Omnetics connector was connected to the implanted female one after unscrewing the headcap. CNAP measurements were performed using this system for 10 days after implantation.

Muscle force tests

Force from the gastrocnemius muscle was evaluated to determine nerve block, following a sciatic nerve exposure as described above. The tibialis anterior (TA) and the extensor digitorum longus (EDL) tendon were cut from the foot distally. Next, a clamp, positioned at the femoral condyles, secured the rat to the force-transducing apparatus. The EDL was secured to a metal S-hook with 5-0 silk suture (Ethicon), which coupled the EDL to a thin-film load cell (S100, Strain Measurement Devices) on a sliding adjustable mount. The Red Rock Laboratories apparatus controlled both stimulation and recordings during acute experimentations. A single pulse (amplitude, 1 mV; burst width, 0.3 s; duration, 50 μs) excited the nerve fibers on the proximal stimulating electrode. Last, the muscle force for several twitches was subsequently measured and quantified from the EDL.

In vivo biocompatibility study

Female CD1 (8-week-old) mice were purchased from Charles River Laboratories. All procedures were approved by the Institutional Animal Care and Use Committee of Northwestern University (protocol IS00005877). The mice were anesthetized with isoflurane gas (~2%), and either HDPE (10 μm thick) or the devices were implanted subcutaneously through a dorsal incision. Before the implantation, exposure to UV radiation overnight sterilized all samples. Daily care including weighing of the mice ensured healthy condition under normal stress exposure. Euthanizing three mice at 2, 4, 6, and 8 weeks after implantation enabled explanting and weighing of major organs (i.e., brain, heart, lung, liver, kidney, and spleen) for histology. Tissues from each organ were fixed in 10% neutral buffered formalin, embedded in paraffin, and sectioned and stained with H&E. Polymorphonuclear cells and lymphocytes were identified by morphology from at least three distinct regions per samples. Histological scores were assessed as reported earlier. Three random locations were chosen for the capsule thickness measurements from optical micrographs. Additional biocompatibility tests consisted of control and experimental groups (time points of months 1, 3, and 6). Experiment began with the purchase of 12 adult male Lewis rats from Charles River Laboratories followed by implantation of devices (all but the control group) in their right hind leg via a sciatic nerve exposure. The samples included a portion of both the nerve contacting the devices and the surrounding muscle. Fixation required placing the nerves in 10% neutral buffered formalin for 48 hours, rinsing with PBS, and then dehydrating incrementally with an ethanol (EtOH) solution with deionized water (DIW) (15 min in 30% EtOH/70% DIW, 15 min in 50% EtOH/50% DIW, final solution of 70% EtOH/30% DIW). After dehydration, all samples were embedded in paraffin, sectioned, stained with H&E, and sealed by microscope cover glasses. The slides were then imaged using a NanoZoomer and examined for signs of immune cell recruitment.

Statistical analysis

Histological and immunohistochemical analyses were quantitatively performed with three samples per each group. Numerical data were converted to means ± SD. Statistical analysis used the Statistical Package for the Social Science (SPSS Statistics, IBM Inc., USA) software. The normality of experimental data was confirmed by the Shapiro-Wilk test, and the statistical analysis was carried out by Student's t test. A P value of > 0.05 was deemed no statistical significance.

SUPPLEMENTARY MATERIALS

Supplementary material for this article is available at https://science.org/doi/10.1126/sciadv.abp9169

View/request a protocol for this paper from *Bio-protocol*.

REFERENCES AND NOTES

1. N. Volkow, H. Benveniste, A. T. McLellan, Use and misuse of opioids in chronic pain. *Annu. Rev. Med.* **69**, 451–465 (2018).
2. C. Florence, F. Luo, L. Xu, C. Zho, The economic burden of prescription opioid overdose, abuse and dependence in the United States, 2013. *Med. Care* **54**, 901–906 (2016).
3. P. Seth, R. A. Rudd, R. K. Noonan, T. M. Haegerich, Quantifying the epidemic of prescription opioid overdose deaths. *Am. J. Public Health* **108**, 500–502 (2018).
4. N. Bhadra, E. Foldes, T. Vrabec, K. Kilgore, N. Bhadra, Temporary persistence of conduction block after prolonged kilohertz frequency alternating current on rat sciatic nerve. *J. Neural Eng.* **15**, 016012 (2018).
5. L. M. Roldan, T. E. Eggers, K. L. Kilgore, N. Bhadra, T. Vrabec, N. Bhadra, Measurement of block thresholds in kilohertz frequency alternating current peripheral nerve block. *J. Neurosci. Methods* **315**, 48–54 (2019).
6. K. L. Kilgore, N. Bhadra, Reversible nerve conduction block using kilohertz frequency alternating current. *Neuromodulation* **17**, 242–255 (2014).
7. M. A. Fishman, A. M. Scherer, A. M. Katsarakes, L. Larson, P. S. Kim, Temperature-mediated nerve blocks in the treatment of pain. *Curr. Pain Headache Rep.* **25**, 60 (2021).
8. D. M. Ackermann, E. L. Foldes, N. Bhadra, K. L. Kilgore, Nerve conduction block using combined thermoelectric cooling and high frequency electrical stimulation. *J. Neurosci. Methods* **193**, 72–76 (2010).
9. Y. F. Lee, C. C. Lin, J.-S. Cheng, G.-S. Chen, Nerve conduction block in diabetic rats using high-intensity focused ultrasound for analgesic applications. *Br. J. Anaesth.* **114**, 840–846 (2015).
10. V. Colucci, G. Strichartz, F. Jolesz, N. Vykhodtseva, K. Hynynen, Focused ultrasound effects on nerve action potential in vitro. *Ultrasound Med. Biol.* **35**, 1737–1747 (2009).
11. E. H. Lothet, K. L. Kilgore, N. Bhadra, N. Bhadra, T. Vrabec, Y. T. Wang, E. D. Jansen, M. W. Jenkins, H. J. Chiel, Alternating current and infrared produce an onset-free reversible nerve block. *Neurophotonics* **1**, 011010 (2014).

12. S. M. Iyer, K. L. Montgomery, C. Towne, S. Y. Lee, C. Ramakrishnan, K. Deisseroth, S. L. Delp, Virally mediated optogenetic excitation and inhibition of pain in freely moving nontransgenic mice. *Nat. Biotechnol.* **32**, 274–278 (2014).
13. I. Jones, M. I. Johnson, Transcutaneous electrical nerve stimulation. *Anaesth. Crit. Care Pain Med.* **9**, 130–135 (2009).
14. M. Johnson, Transcutaneous electrical nerve stimulation: Mechanisms, clinical application and evidence. *Rev. Pain* **1**, 7–11 (2007).
15. A. M. Cobo, C. E. Larson, K. Scholten, J. A. Miranda, S. Elyahoodayan, D. Song, V. Pikov, E. Meng, Parylene-based cuff electrode with integrated microfluidics for peripheral nerve recording, stimulation, and drug delivery. *J. Microelectromech. Syst.* **28**, 36–49 (2019).
16. B. M. Ilfeld, E. T. Said, J. J. Finneran IV, J. F. Sztain, W. B. Abramson, R. A. Gabriel, B. Khatibi, M. W. Swisher, P. Jaeger, D. C. Covey, C. M. Robertson, Ultrasound-guided percutaneous peripheral nerve stimulation: Neuromodulation of the femoral nerve for postoperative analgesia following ambulatory anterior cruciate ligament reconstruction: A proof of concept study. *Neuromodulation* **22**, 621–629 (2019).
17. M. Rossi, G. D. Carolis, G. Liberatoscioli, D. Iemma, P. Nosella, L. F. Nardi, A novel mini-invasive approach to the treatment of neuropathic pain: The PENS study. *Pain Physician* **19**, E121–E128 (2016).
18. T. Eggers, J. Kilgore, D. Green, T. Vrabec, K. Kilgore, N. Bhadra, Combining direct current and kilohertz frequency alternating current to mitigate onset activity during electrical nerve block. *J. Neural Eng.* **18**, 046010 (2021).
19. N. Bhadra, T. L. Vrabec, N. Bhadra, K. L. Kilgore, Reversible conduction block in peripheral nerve using electrical waveforms. *Bioelectron. Med.* **1**, 39–54 (2018).
20. E. L. Foldes, D. M. Ackermann, N. Bhadra, K. L. Kilgore, Counted cycles method to quantify the onset response in high-frequency peripheral nerve block, in *2009 Annual International Conference of the IEEE Engineering in Medicine and Biology Society* (IEEE, 2009), pp. 614–617.
21. N. Bhadra, K. L. Kilgore, High-frequency electrical conduction block of mammalian peripheral motor nerve. *Muscle Nerve* **32**, 782–790 (2005).
22. M.-A. Thil, D. T. Duy, I. M. Colin, J. Delbeke, Time course of tissue remodelling and electrophysiology in the rat sciatic nerve after spiral cuff electrode implantation. *J. Neuroimmunol.* **185**, 103–114 (2007).
23. Y. Liu, J. Liu, S. Chen, T. Lei, Y. Kim, S. Niu, H. Wang, X. Wang, A. M. Foudeh, J. B.-H. Tok, Z. Bao, Soft and elastic hydrogel-based microelectronics for localized low-voltage neuromodulation. *Nat. Biomed. Eng.* **3**, 58–68 (2019).
24. G. Lee, Y. S. Choi, H.-J. Yoon, J. A. Rogers, Advances in physicochemically stimuli-responsive materials for on-demand transient electronic systems. *Matter* **3**, 1031–1052 (2020).
25. J.-Y. Bae, S.-G. Choi, J.-Y. Lee, S.-K. Kang, Silicon transient electronics: Bioresorbable to hardware-secure device. *Proc. SPIE* **10982**, 109821U (2019).
26. C. You, H. Zhao, Q. Guo, Y. Mei, Material strategies for on-demand smart transient electronics. *MRS Bulletin* **45**, 129–134 (2020).
27. H. Guo, D. D'Andrea, J. Zhao, Y. Xu, Z. Qiao, L. E. Janes, N. K. Murthy, R. Li, Z. Xie, Z. Song, R. Meda, J. Koo, W. Bai, Y. S. Choi, S. W. Jordan, Y. Huang, C. K. Franz, J. A. Rogers, Advanced materials in wireless, implantable electrical stimulators that offer rapid rates of bioresorption for peripheral axon regeneration. *Adv. Funct. Mater.* **31**, 2102724 (2021).
28. J. Koo, M. R. MacEwan, S.-K. Kang, S. M. Won, M. Stephen, P. Gamble, Z. Xie, Y. Yan, Y.-Y. Chen, J. Shin, N. Birenbaum, S. Chung, S. B. Kim, J. Khalifeh, D. V. Harburg, K. Bean, M. Paskett, J. Kim, Z. S. Zohny, S. M. Lee, R. Zhang, K. Luo, B. Ji, A. Banks, H. M. Lee, Y. Huang, W. Z. Ray, J. A. Rogers, Wireless bioresorbable electronic system enables sustained nonpharmacological neuroregenerative therapy. *Nat. Med.* **24**, 1830–1836 (2018).
29. S.-K. Kang, R. K. J. Murphy, S.-W. Hwang, S. M. Lee, D. V. Harburg, N. A. Krueger, J. Shin, P. Gamble, H. Cheng, S. Yu, Z. Liu, J. G. McCall, M. Stephen, H. Ying, J. Kim, G. Park, R. C. Webb, C. H. Lee, S. Chung, D. S. Wie, A. D. Gujar, B. Vemulapalli, A. H. Kim, K.-M. Lee, J. Cheng, Y. Huang, S. H. Lee, P. V. Braun, W. Z. Ray, J. A. Rogers, Bioresorbable silicon electronic sensors for the brain. *Nature* **530**, 71–76 (2016).
30. M. A. Hamza, E.-S. A. Ghoname, P. F. White, W. F. Craig, H. E. Ahmed, N. M. Gajraj, A. S. Vakharia, C. E. Noe, Effect of the duration of electrical stimulation on the analgesic response in patients with low back pain. *Anesthesiology* **91**, 1622–1627 (1999).
31. S.-K. Kang, S.-W. Hwang, S. Yu, J.-H. Seo, E. A. Corbin, J. Shin, D. S. Wie, R. Bashir, Z. Ma, J. A. Rogers, Biodegradable thin metal foils and spin-on glass materials for transient electronics. *Adv. Funct. Mater.* **25**, 1789–1797 (2015).
32. D. Lu, Y. Yan, R. Avila, I. Kandela, I. Stepien, M.-H. Seo, W. Bai, Q. Yang, C. Li, C. R. Haney, E. A. Waters, M. R. MacEwan, Y. Huang, W. Z. Ray, J. A. Rogers, Bioresorbable, wireless, passive sensors as temporary implants for monitoring regional body temperature. *Adv. Healthc. Mater.* **9**, e2000942 (2020).
33. S. M. Won, J. Koo, K. E. Crawford, A. D. Mickle, Y. Xue, S. Min, L. A. McIlvried, Y. Yan, S. B. Kim, S. M. Lee, B. H. Kim, H. Jang, M. R. MacEwan, Y. Huang, R. W. Gereau, J. A. Rogers, Natural wax for transient electronics. *Adv. Funct. Mater.* **28**, 1–10 (2018).
34. D. M. Ackermann, N. Bhadra, E. L. Foldes, X.-F. Wang, K. L. Kilgore, Effect of nerve cuff electrode geometry on onset response firing in high-frequency nerve conduction block. *IEEE Trans. Neural Syst. Rehabil. Eng.* **18**, 658–665 (2010).
35. D. M. Ackermann, E. L. Foldes, N. Bhadra, K. L. Kilgore, Effect of bipolar cuff electrode design on block thresholds in high-frequency electrical neural conduction block. *IEEE Trans. Neural Syst. Rehabil. Eng.* **17**, 469–477 (2009).
36. N. Julémont, A. Nonclercq, A. Delchambre, A. Vanhoestenberghe, A study on cross-talk nerve stimulation: Electrode placement and current leakage lid. *Eur. J. Transl. Myol.* **26**, 239–243 (2016).
37. R. A. Gaunt, A. Prochazka, Transcutaneously coupled, high-frequency electrical stimulation of the pudendal nerve blocks external urethral sphincter contractions. *Neurorehabil. Neural Repair* **23**, 615–626 (2009).
38. Y. S. Choi, J. Koo, Y. J. Lee, G. Lee, R. Avila, H. Ying, J. Reeder, L. Hambitzer, K. Im, J. Kim, K.-M. Lee, J. Cheng, Y. Huang, S. K. Kang, J. A. Rogers, Biodegradable polyanhydrides as encapsulation layers for transient electronics. *Adv. Funct. Mater.* **30**, 2000941 (2020).
39. Y. S. Choi, R. T. Yin, A. Pfenniger, J. Koo, R. Avila, K. B. Lee, S. W. Chen, G. Lee, G. Li, Y. Qiao, A. Murillo-Berlioz, A. Kiss, S. Han, S. M. Lee, C. Li, Z. Xie, Y.-Y. Chen, A. Burrell, B. Geist, H. Jeong, J. Kim, H.-J. Yoon, A. Banks, S.-K. Kang, Z. J. Zhang, C. R. Haney, A. V. Sahakian, D. Johnson, T. Efimova, Y. Huang, G. D. Trachiotis, B. P. Knight, R. K. Arora, I. R. Efimov, J. A. Rogers, Fully implantable and bioresorbable cardiac pacemakers without leads or batteries. *Nat. Biotechnol.* **39**, 1228–1238 (2021).
40. Y. Gao, Y. Zhang, X. Wang, K. Sim, J. Liu, J. Chen, X. Feng, H. Xu, C. Yu, Moisture-triggered physically transient electronics. *Sci. Adv.* **3**, e1701222 (2017).
41. Y. S. Choi, Y. Y. Hsueh, J. Koo, Q. Yang, R. Avila, B. Hu, Z. Xie, G. Lee, Z. Ning, C. Liu, Y. Xu, Y. J. Lee, W. Zhao, J. Fang, Y. Deng, S. M. Lee, A. Vázquez-Guardado, I. Stepien, Y. Yan, J. W. Song, C. Haney, Y. S. Oh, W. Liu, H.-J. Yoon, A. Banks, M. R. MacEwan, G. A. Ameer, W. Z. Ray, Y. Huang, T. Xie, C. K. Franz, S. Li, J. A. Rogers, Stretchable, dynamic covalent polymers for soft, long-lived bioresorbable electronic stimulators designed to facilitate neuromuscular regeneration. *Nat. Commun.* **11**, 5990 (2020).
42. E. Vey, C. Rodger, L. Meehan, J. Booth, M. Claybourn, A. F. Miller, A. Saiani, The impact of chemical composition on the degradation kinetics of poly(lactic-co-glycolic) acid copolymers cast films in phosphate buffer solution. *Polym. Degrad. Stabil.* **97**, 358–365 (2012).
43. J. M. Cuellar, K. Alataris, A. Walker, D. C. Yeomans, J. F. Antognini, Effect of high-frequency alternating current on spinal afferent nociceptive transmission. *Neuromodulation* **16**, 318–327 (2013).
44. C. Boehler, S. Carli, L. Fadiga, T. Stieglitz, M. Asplund, Tutorial: Guidelines for standardized performance tests for electrodes intended for neural interfaces and bioelectronics. *Nat. Protocols* **15**, 3557–3578 (2020).
45. M. Ganji, A. Tanaka, V. Gilja, E. Halgren, S. A. Dayeh, Scaling effects on the electrochemical stimulation performance of Au, Pt, and PEDOT:PSS electrocorticography arrays. *Adv. Funct. Mater.* **27**, 1703019 (2017).
46. S. Negi, R. Bhandari, L. Rieth, F. Solzbacher, In vitro comparison of sputtered iridium oxide and platinum-coated neural implantable microelectrode arrays. *Biomed. Mater.* **5**, 15007 (2010).
47. S. F. Cogan, Neural stimulation and recording electrodes. *Annu. Rev. Biomed. Eng.* **10**, 275–309 (2008).
48. W. Cairang, T. Li, D. Xue, H. Yang, P. Cheng, C. Chen, Y. Sun, Y. Zeng, X. Ding, J. Sun, Enhancement of the corrosion resistance of molybdenum by La_2O_3 dispersion. *Corrosion Sci.* **186**, 109469 (2021).
49. J. K. Trevathan, I. W. Baumgart, E. N. Nicolai, B. A. Gosink, A. J. Asp, M. L. Settell, S. R. Polaconda, K. D. Malerick, S. K. Brodnick, W. Zeng, B. E. Knudsen, A. L. McConico, Z. Sanger, J. H. Lee, J. M. Aho, A. J. Suminski, E. K. Ross, J. L. Lujan, D. J. Weber, J. C. Williams, M. Franke, K. A. Ludwig, A. J. Shoffstall, An injectable neural stimulation electrode made from an in-body curing polymer/metal composite. *Adv. Healthc. Mater.* **8**, e1900892 (2019).
50. G. Lee, S.-K. Kang, S. M. Won, P. Gutruf, Y. R. Jeong, J. Koo, S.-S. Lee, J. A. Rogers, J. S. Ha, Fully biodegradable microsupercapacitor for power storage in transient electronics. *Adv. Energy Mater.* **7**, 1700157 (2017).
51. H. Lee, G. Lee, J. Yun, K. Keum, S. Y. Hong, C. Song, J. W. Kim, J. H. Lee, S. Y. Oh, D. S. Kim, M. S. Kim, J. S. Ha, Facile fabrication of a fully biodegradable and stretchable serpentine-shaped wire supercapacitor. *Chem. Eng. J.* **366**, 62–71 (2019).
52. S. Naghdi, K. Nešović, V. Mišković-Stanković, K. Y. Rhee, Comprehensive electrochemical study on corrosion performance of graphene coatings deposited by chemical vapour deposition at atmospheric pressure on platinum-coated molybdenum foil. *Corrosion Sci.* **130**, 31–44 (2018).
53. X. S. Zheng, C. Tan, E. Castagnola, X. T. Cui, Electrode materials for chronic electrical microstimulation. *Adv. Healthc. Mater.* **10**, 2100119 (2021).
54. S. P. Lacour, G. Courtine, J. Guck, Materials and technologies for soft implantable neuroprostheses. *Nat. Rev. Mater.* **1**, 16063 (2016).

55. L. K. Jones, Nerve conduction studies: Basic concepts and patterns of abnormalities. *Neurol. Clin.* **30**, 405–427 (2012).
56. A. Mallik, A. I. Weir, Nerve conduction studies: Essentials and pitfalls in practice. *Neurol. Pract.* **76**, ii23–ii31 (2005).
57. R. Sahyouni, A. Mahmoodi, J. W. Chen, D. T. Chang, O. Moshtaghi, H. R. Djalilian, H. W. Lin, Interfacing with the nervous system: A review of current bioelectric technologies. *Neurosurg. Rev.* **42**, 227–241 (2019).
58. L. Yin, H. Cheng, S. Mao, R. Haasch, Y. Liu, X. Xie, S. W. Hwang, H. Jain, S. K. Kang, Y. Su, R. Li, Y. Huang, J. A. Rogers, Dissolvable metals for transient electronics. *Adv. Funct. Mater.* **24**, 645–658 (2014).
59. J. Tao, J. Zhang, T. Du, X. Xu, X. Deng, S. Chen, J. Liu, Y. Chen, X. Liu, M. Xiong, Y. Luo, H. Cheng, J. Mao, L. Cardon, M. Gou, Y. Wei, Rapid 3D printing of functional nanoparticle-enhanced conduits for effective nerve repair. *Acta Biomater.* **90**, 49–59 (2019).
60. M. Salehi, Z. Bagher, S. K. Kamrava, A. Ehterami, R. Alizadeh, M. Farhadi, M. Falah, A. Komeili, Alginate/chitosan hydrogel containing olfactory ectomesenchymal stem cells for sciatic nerve tissue engineering. *J. Cell. Physiol.* **234**, 15357–15368 (2019).

Acknowledgments: We thank Y. Xu (Washington University, St. Louis) for the help in electrophysiology tests and N. Ghoreishi-Haack, E. Dempsey, I. Stepien, and C. Haney (Northwestern University) for the help in biocompatibility studies and imaging. **Funding:** This work was supported by the Querrey Simpson Institute for Bioelectronics. Histology services were provided by the Northwestern University Mouse Histology and Phenotyping Laboratory, which is supported by NCI P30-CA060553 awarded to the Robert H. Lurie Comprehensive Cancer Center. G.L. acknowledges support from the Korea Institute for Advancement of Technology grant funded by the Korea Government (MOTIE) [P0017305, Human Resource Development Program for Industrial Innovation (Global)]. Y.S.C. acknowledges support from the NIH (grant 1K99HL155844-01A1). S.Ş. acknowledges support from the Turkish Fulbright Commission under Fulbright Postdoctoral Program (FY-2020-TR-PD-10). M.R.M. acknowledges support from the Office of the Assistant Secretary of Defense for Health Affairs through the Peer Reviewed Orthopedic Research Program (award no. W81XWH-17-PRORP-ARA). **Author contributions:** Conceptualization: G.L., M.R.M., and J.A.R. Investigation: G.L., E.R., H.-J.Y., S.G., Y.S.C., M.-K.L., S.Ş., H.-Y.A., J.K., M.P., H.R., S.S.K., Y.H.J., A.O., U.K., and W.Z.R. Methodology: G.L., M.-K.L., S.Ş., Y.Y., and A.J.B. Fabrication: G.L., H.-J.Y., and H.-Y.A. Visualization: G.L. Supervision: M.R.M. and J.A.R. Writing—original draft: G.L., E.R., H.-J.Y., S.G., and J.A.R. Writing—review and editing: G.L., E.R., S.G., Y.S.C., S.Ş., A.J.B., M.R.M., and J.A.R. **Competing interests:** The authors declare that they have no competing interests. **Data and materials availability:** All data needed to evaluate the conclusions in the paper are present in the paper and/or the Supplementary Materials.

Submitted 8 March 2022
Accepted 18 August 2022
Published 5 October 2022
10.1126/sciadv.abp9169